



Science Arts & Métiers (SAM)

is an open access repository that collects the work of Arts et Métiers Institute of Technology researchers and makes it freely available over the web where possible.

This is an author-deposited version published in: <https://sam.ensam.eu>
Handle ID: <http://hdl.handle.net/10985/21436>

To cite this version :

Belkacem MANSER, Idir BELAIDI, Abderrachid HAMRANI, Farid BAKIR, Sofiane KHELLADI - Texture shape effects on hydrodynamic journal bearing performances using mass-conserving numerical approach - Tribology - Materials Surfaces & Interfaces - Vol. 14, n°1, p.33-50 - 2019

Any correspondence concerning this service should be sent to the repository

Administrator : scienceouverte@ensam.eu



Texture shape effects on hydrodynamic journal bearing performances using mass-conserving numerical approach

B. Manser ^a, I. Belaidi ^a, A. Hamrani ^b, S. Khelladi ^c and F. Bakir ^c

^aLEMI, FSI, University of M'hamed Bougara, Boumerdes, Algeria; ^bDepartment of Bioresource Engineering, McGill University, Montreal, Canada; ^cDynFluid Lab., Arts et Métiers ParisTech, Paris, France

ABSTRACT

It is a known fact that incorporating textures in the contact surfaces can significantly enhance bearing performances. The purpose of this paper is to outline the effects of texture bottom profiles and contour geometries on the performances of hydrodynamic textured journal bearings. The analysis was conducted using computational approach to test eight texture shapes: rectangular, cylindrical, spherical, triangular (TR, T1, T2, T3) and chevron. The steady-state Reynolds equation for modelling the hydrodynamic behaviour of thin viscous film was solved using finite difference technique and mass conservation algorithm (JFO boundary conditions), taking into account the presence of textures on both full film and cavitation regions. The comparison with the benchmark data shows good consistency and an enhancement in bearing performances (load carrying capacity and friction). The results clearly show that the mechanisms of wedge effect and micro-step bearing for the full/partial texturing feature are the main crucial parameters, where the convergent wedge effect present in T2 triangular texture shape can significantly enhance the load-carrying capacity, while the divergent wedge action causes a net load loss. Considering the right arrangement of textures on the contact surface, their surface contours can have a significant impact on the performance of hydrodynamic journal bearings at high eccentricity ratios.

KEYWORDS

Hydrodynamic journal bearing; surface texturing; bottom profile; contour geometry; wedge effect; dimple shapes

1. Introduction

The industrial world is currently facing a challenge where the economic conditions are restricted, due to the rise in energy prices, and environmental requirements. Consequently, many researches are often directed towards the optimization of existing systems, reducing energy consumption and increasing performance. It is well known that the performances of any machine are directly influenced by its effectiveness in terms of friction, which is the main cause of wear and energy losses. For example, in the automobile industry, more than one-quarter of the consumed energy is used to overcome the friction between components [1]. This fact is similar in other industrial sectors, such as aeronautics field. The study of these tribological aspects, i.e. friction, lubrication, wear and contact mechanics, becomes fundamental. Moreover, the technological progress that has been achieved in recent years, allows for a precise control of the surface properties (roughness, grooves, discrete textures/dimples). The technique of surface texturing is commonly used to control the tribological performances of the considered system. The idea is originated from the roughness, but in the case of surface texturing, the operator intentionally incorporate a well defined dimple shape to obtain the desired tribological characteristics [2]. Textured surfaces are characterized by various geometrical parameters such

as shape, size, area density and orientation distribution of the pattern. For composing the specific types of texture patterns, there are various well-known shapes such as rectangular, cylindrical, spherical, sinusoidal, triangular, elliptical, chevron, etc, which are commonly used in published literature [3]. There is a wide range of industrial techniques that can be used for manufacturing this surface texture, such as laser surface texturing [4], reactive ion etching [5], LIGA process (lithography, moulding and electroplating) [6], vibro-rolling [7], vibro-mechanical texturing [8] and abrasive jet machining [9].

Surface texturing have many functionalities, e.g. in the seals industry, this technology is applied to minimize friction and leakage in mechanical [10]/gas seals [11,12], in the automotive industry, it is used to reduce friction of piston rings [13]. Furthermore, surface texturing has proved to be very effective in all lubrication regimes, particularly in the case of hydrodynamic bearing systems [5], where it is employed to improve the load carrying capacity by providing supplementary hydrodynamic pressure [14], acting as lubricant reservoirs to ensure supply in cases of lubricant starvation [15,16], entrapping wear debris and abrasive particles to prevent severe wear [17–21].

The study of textured journal bearing has been the object of numerous theoretical and experimental

studies. Lu and Khonsari [22] presented a series of experimental results to examine the effect of fully and partially textured journal bearings on the Stribeck curve. They explored the effect of external force, oil type and texture parameters on the friction characteristics. It was shown that the friction coefficient in fully textured bearing, can be reduced, with the appropriate selection of texture size, depth and density. One of the first works focusing on the numerical aspect of textured journal bearings was conducted by Tala-Ighil et al. [23,24], where they used a finite difference model to solve the two-dimensional Reynolds equation under steady-state conditions. Their objective was to investigate the effect of the spherical and cylindrical shapes on the bearing performance, where it was reported that textured surface affected the main bearing characteristics. Depending on the dimple parameters (size, depth, density and distribution), texturing can exert positive or negative effects. Further, they reported, that the partial texturing configuration including the texturing of multiple zones has a positive influence on hydrodynamic contact characteristics. Another study was presented by Ausas et al. [25], where they numerically investigated the impact of the cavitation model on the performance of textured journal bearings. A comparison was made between results obtained from the classical Reynolds model and the mass conserving algorithm proposed by Elrod and Adams [26] for fully textured journal bearings with rectangular dimples. A slight increase in the minimum film thickness and friction torque was observed. Another, numerical study, performed by Kango et al. [27,28], shows the combined influences of viscous heat dissipation and non-Newtonian rheology of lubricant on the performance of textured journal bearings. Spherical dimples using mass conservation algorithm and oil mixing temperature concepts were used. The finite difference technique for solving the Reynolds and energy equations was adopted. It was noticed a reduction in average temperature of the lubricant in the presence of surface texturing in comparison to smooth surface of the bearing. Zhang et al. [29] presented a parametric design of the surface texturing on the journal bearing, with the aim of achieving the optimal textures distribution for improving the load capacity.

To explain the behaviour of the lubricant inside the micro-textured surfaces, several mechanisms have been proposed. The most common mechanisms were: the 'micro-wedge action' [14,30], the 'collective dimple effect' [31], the 'inlet roughness' [32,33], the 'load support mechanism' [34,35], and the 'balancing wedge action' [36]. Based on these mechanisms, Nanbu et al. [37] reported that textures with bottom shapes containing a micro-wedge and/or a micro-step bearing tend to increase film thicknesses and pressure lift. Recently, Uddin et al. [38] investigated the effects of

surface texture shape, geometry, bottom profile, orientation, depth and density on the tribological performances of parallel rotating thrust bearings. It was mentioned that considerable improvement in the bearing performance is achieved by texture shapes with micro-wedge and/or micro-step features.

The above-mentioned works show that, the tribological performances of textured surfaces are very sensitive to the texture mechanism. Indeed, some dimple shapes with micro-wedge and/or micro-step features perform better by increasing the load lifting capacity and lowering the friction force. No systematic study dealing with the wedge effect and/or contour geometries of texture shapes on the particular case of journal bearing appears to exist in the open literature. Thus, the objective of this numerical study is to bring elements of a response to the questions related to the effect of texture contour geometries and bottom profiles on the main journal bearing characteristics (i.e. film thicknesses, pressure distribution, load carrying capacity, friction coefficient, side leakage, etc), using Elrod's efficient mass conservation algorithm for implementation the JFO boundary conditions.

The content of this paper is organized as follows : Section 2 provides the description of the modified Reynolds equation, cavitation boundary condition and the computational procedure. Section 3 is devoted to the numerical results and discussions, which contains the preliminary validation and performance analysis. Finally, conclusions are given in the last section.

2. Governing equations for hydrodynamic journal bearing

2.1. Reynolds equation and Elrod cavitation algorithm

In the lubrication theory, Reynolds equation is employed for the computation of the pressure distribution of thin viscous fluid films. Based on the assumptions [1] that : the fluid is Newtonian; isoviscous and incompressible under laminar flow, the Reynolds equation for a journal operating at steady state regime (in Cartesian coordinates), can be written as:

$$\frac{\partial}{\partial x} \left(\frac{1}{12} \rho h^3 \frac{\partial p}{\partial x} \right) + \frac{\partial}{\partial z} \left(\frac{1}{12} \rho h^3 \frac{\partial p}{\partial z} \right) = \frac{1}{2} \mu U \frac{\partial(\rho h)}{\partial x} \quad (1)$$

where p : lubricant pressure, h : film thickness, μ : dynamic viscosity, ρ : lubricant density and U : shaft speed.

In the full film zone, the density is constant and Equation (1) becomes:

$$\frac{\partial}{\partial x} \left(\frac{1}{12} h^3 \frac{\partial p}{\partial x} \right) + \frac{\partial}{\partial z} \left(\frac{1}{12} h^3 \frac{\partial p}{\partial z} \right) = \frac{1}{2} \mu U \frac{\partial h}{\partial x} \quad (2)$$

In rupture zone, the pressure remains constant at the cavitation pressure. Hence, Equation (1) is

reduced to:

$$\frac{\partial}{\partial x} \left(\frac{\rho h U}{2} \right) = 0 \quad (3)$$

In order to take into account the effect of film rupture and reformation, Jakobsson, Floberg [39] and Olsson [40] proposed the so-called JFO boundary conditions. The JFO boundary condition have been added to be more realistic then Reynolds boundary condition and sufficiently accurate model to account for lubricant cavitation, especially in: misaligned, dynamical-loaded and textured bearings [25,27,41].

To use the JFO boundary conditions, Elrod [26] suggested to combination of the two Equations (2) and (3) into a single 'universal' equation that covers both the cavitated and the full film regions, by introducing a new parameter called fractional film content $= \rho/\rho_c$, where ρ_c is the cavitated oil density.

The resulting mass conservative form of the Reynolds equation where the unknown is the factional film content instead of the pressure can be written as follows:

$$\begin{aligned} \frac{\partial}{\partial x} \left(\frac{1}{12} \beta h^3 g \frac{\partial \Theta}{\partial x} \right) + \frac{\partial}{\partial z} \left(\frac{1}{12} \beta h^3 g \frac{\partial \Theta}{\partial z} \right) \\ = \frac{1}{2} \mu U \frac{\partial(\Theta h)}{\partial x} \end{aligned} \quad (4)$$

where β is the bulk modulus which represents the variation of the lubricant compressibility in the full film region and the pressure p is given by:

$$\beta = \rho \frac{\partial p}{\partial \rho} \quad (5)$$

and $g(\Theta)$ is the switch function (cavitation index) which is zero in the cavitation zone and equal to unity in the full film zone.

$$\begin{aligned} g &= 1 & \text{if } \Theta \geq 1 \\ g &= 0 & \text{if } \Theta < 1 \end{aligned} \quad (6)$$

After solving Equation (4) for Θ , the pressure in the full film region can be determined using the following relation [26]:

$$p = p_c + g\beta \ln(\Theta) \quad (7)$$

where, p_c is the cavitation pressure.

By introducing the following dimensionless parameters:

$$\theta = x/R \quad Z = z/L \quad \bar{h} = h/C \quad \bar{y} = y/h \quad \bar{\beta} = \frac{\beta C^2}{UR}$$

where, R : bearing radius, L : bearing length and C : radial clearance.

The dimensionless form of the modified Reynolds equation becomes:

$$\begin{aligned} \frac{1}{12} \frac{\partial}{\partial \theta} \left(\bar{\beta} g \bar{h}^3 \frac{\partial \Theta}{\partial \theta} \right) + \left(\frac{R}{L} \right)^2 \frac{1}{12} \frac{\partial}{\partial Z} \left(\bar{\beta} g \bar{h}^3 \frac{\partial \Theta}{\partial Z} \right) \\ = \frac{1}{2} \frac{\partial(\Theta \bar{h})}{\partial \theta} \end{aligned} \quad (8)$$

and the dimensionless pressure is described by:

$$\bar{P} = \bar{P}_c + g\bar{\beta} \ln(\Theta) \quad (9)$$

where dimensionless film thickness is described by:

$$\bar{h}_{(\theta,Z)} = \bar{h}_{Smooth(\theta)} + \bar{\Delta h}_{(\theta,Z)} \quad (10)$$

where, $\bar{h}_{Smooth(\theta)}$ denotes the smooth part of the film geometry ($\bar{h}_{Smooth(\theta)} = 1 + \varepsilon \cos \theta$) and $\bar{\Delta h}_{(\theta,Z)}$ is the part due to the textured surface, it characterizes the depth of the fluid film in the texture (Figure 1).

2.2. Texture shapes, geometries and configurations

In general, textures can be characterized by their shape (contour geometry, bottom profile), size (contour dimension, depth), number (along axial/circumferential directions), density and distribution. Based on textured thrust pad bearing studies reported in the literature, Zhang et al. [42] demonstrated that, square texture shape performed the best hydrodynamic enhancement, followed by the triangle, circle and rectangle. While, Uddin et al. [38] showed that texture shapes with convergent (positive) wedge bottom profile offer the best performance, while, texture shapes with divergent (negative) wedge bottom profile perform the worst. According to that reasoning, in this study, eight different texture shapes are considered and grouped into two main categories. Four texture shapes with constant dimple depth or flat bottom ($\bar{\Delta h} = cst$): square, cylindrical, triangular and chevron fall within the first category. The second category concerns another four texture shapes with variable dimple depth or wedge bottom ($\bar{\Delta h} \neq cst$): T1, T2, T3 and spherical. It should be emphasized that the first category is chosen to highlight the effect of texture contour geometries at the bearing surface and the second one to examine the effect of bottom shape profiles. Texture geometries, parameters and equations are summarized in Tables 1 and 2, respectively. The coordinates of the texture centre C are noted (x_c, y_c, z_c) . This centre is located on the bearing surface, making $y_c = 0$. Texture dimensional parameters are r_x , r_y and r_z in the x , y , and z directions, respectively.

Tala-Ighil et al. [43] simulated 25 cases of cylindrical texture shape with different texture distributions including full texturing and partial

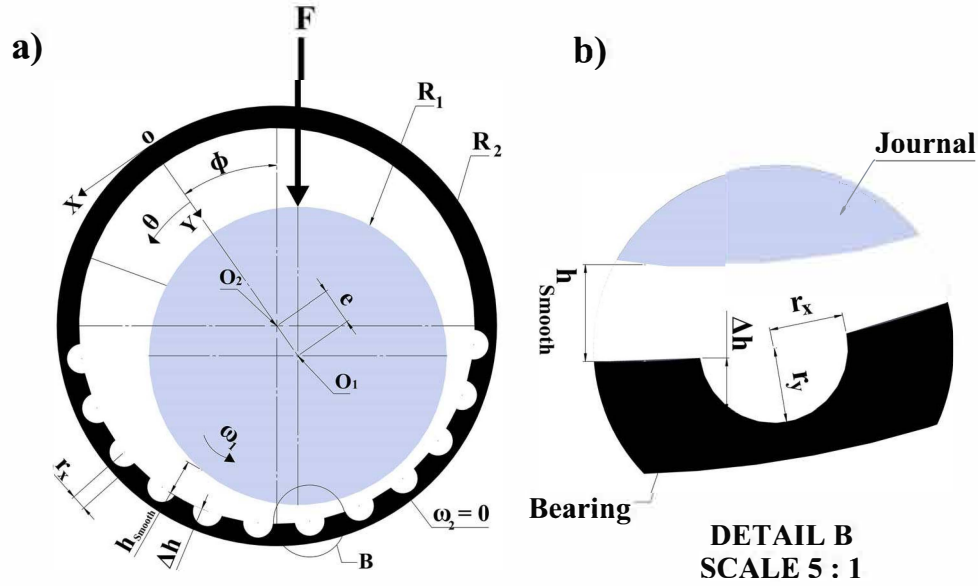


Figure 1. Representative scheme of: (a) straight section of the textured journal bearing; (b) detailed section for the texture scheme.

texturing with one or multiple separated zones of the bearing surface. They reported that, in one side, full texturing have a detrimental effect, and the partial

texturing, in the other side, has a positive influence. Furthermore, they reported that, the optimal region where texturing can provide more efficiency is

Table 1. Texture profiles and geometric equations four shapes with flat bottom profiles (adapted from [2]).

Description	Texture shapes	Geometric Equations
Square 'SQ'		$\text{if } \begin{cases} -r_x \leq x \leq r_x \\ -r_z \leq z \leq r_z \end{cases} \Rightarrow \Delta h_{(\theta,z)} = r_y$
Cylinder 'CY'		$\text{if } \begin{cases} r_x = r_z = r \\ (x - x_c)^2 + (z - z_c)^2 = r^2 \end{cases} \Rightarrow \Delta h_{(\theta,z)} = r_y$
Triangle 'TR'		$\text{if } \begin{cases} -r_x \leq x \leq r_x \\ \frac{r_x}{2} \leq z \leq -\frac{r_x}{2}x + r_x \end{cases} \Rightarrow \Delta h_{(\theta,z)} = r_y$
Chevron 'CH'		$\text{if } \begin{cases} -r_x \leq x \leq r_x \\ -r_z \leq z \leq r_z \end{cases} \Rightarrow \Delta h_{(\theta,z)} = \begin{cases} r_y & \text{if } \frac{r_x}{2r_x}x \leq z \leq -\frac{r_x}{2r_x}x + r_x \\ r_y & \text{if } -\frac{r_x}{2r_x}x + r_x - r_x \leq z \leq -\frac{r_x}{2r_x}x + r_x \\ 0 & \text{else} \end{cases}$

Table 2. Texture profiles and geometric equations for shapes with wedge bottom profiles (adapted from [37]).

Description	Texture shape	Geometric Equations
T1		$\text{if } \begin{cases} -r_x \leq x \leq r_x \\ -r_z \leq z \leq r_z \end{cases} \Rightarrow \Delta h_{(\theta,z)} = \frac{-2r_y}{r_x} x + r_y$
T2		$\text{if } \begin{cases} -r_x \leq x \leq r_x \\ -r_z \leq z \leq r_z \end{cases} \Rightarrow \Delta h_{(\theta,z)} = -\frac{r_y}{r_x} x + r_y$
T3		$\text{if } \begin{cases} -r_x \leq x \leq r_x \\ -r_z \leq z \leq r_z \end{cases} \Rightarrow \Delta h_{(\theta,z)} = \frac{r_y}{r_x} x$
Sphere 'SP'		$\text{if } \begin{cases} r_x = r_z = r \\ \frac{(x-x_c)^2}{r_x^2} + \frac{(\Delta h - y_c)^2}{r_y^2} + \frac{(z-z_c)^2}{r_z^2} = 1 \end{cases} \Rightarrow \Delta h_{(\theta,z)} = r_y \sqrt{1 - \frac{(x-x_c)^2}{r_x^2} - \frac{(z-z_c)^2}{r_z^2}}$

located at the second half of bearing surface, where the area under the declining part of the pressure field is situated. In this study, two texture configurations, as shown in Figure 2, are considered.

Dobrica et al. [44] studied fully and partially textured parallel slider bearings by applying a two-dimensional mass-conserving form of the Reynolds equation. They showed that, in one hand, the fully textured surface can only generate load carrying capacities when the inlet is textured, on the other hand, the partially textured sliders are capable of creating substantial hydrodynamic lift, especially when the supply pressure is higher than the cavitation pressure and textures are placed at the inlet. Furthermore, they demonstrated that the texture density cannot be optimized for the partially textured sliders, because the load carrying capacity always increases with density, resulting in an optimum density of 100%. However, a density of 100% actually results in a stepped slider and the term texture becomes questionable. In practice, that means that the optimal

texture density is the maximum achievable, limited by the fact that high densities may lead to stress concentration, weakening the surface. In this paper, four densities (20%, 40%, 60% and 80%) are considered.

2.3. Numerical procedure

Based on the mass conservation algorithm (JFO boundary conditions), the approach proposed by Vijayaraghavan and Keith [41] is used herein. The finite differences method with Gauss-Seidel iterative process (successive over-relaxation 'SOR') is employed to compute the fractional film content (θ). Usually, an iterative loop with a convergence criterion is required when JFO boundary conditions are imposed [25]. Moreover, this method is very easy to implement which makes it the preferred solver for small and medium-sized problems [45]. In order to improve the convergence speed and avoid the problem in stabilizing the cavitation zone, the

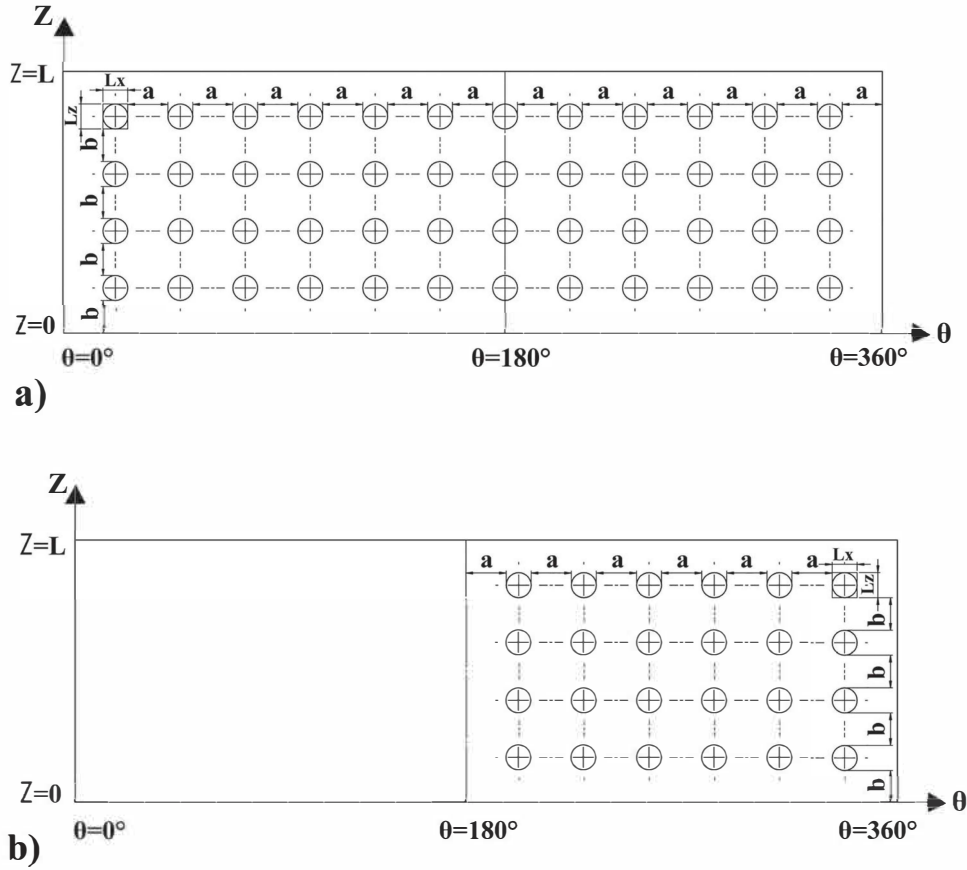


Figure 2. Illustration of textures distribution in the circumferential and axial directions on the bearing surface: (a) full textured case (0° to 360°); (b) partial textured case (180° to 360°).

modified switch function algorithm developed by Fesanghary and Khonsari [45] is used in the computational code, where the 'gfactor' is chosen from the range of 0 to 0.9, and then, the dimensionless pressure field in the full film region can be determined using the Equation (9).

The computational process consists of:

- Introduction of input data: geometrical parameters (L , D , C , and e), operating conditions (N , μ and β), texturing parameters (nC_θ , nC_z , r_x , r_z , r_y , θ_1 , θ_2 , z_1 and z_2) and grid size and convergence criteria;
- Input initial values of: fractional film content $\Theta_{(\theta,Z)}^0$ and binary switch function $g_{(\theta,Z)}^0$;
- Compute the film thickness using Equation (10);
- Solve the modified Reynolds Equation (8);
- Imposition of JFO boundary conditions on affected nodes (Equation (6));
- The fractional film content is obtained by verifying the following convergence condition: $\frac{|\Delta\Theta_{ij}|}{\Theta_{ij}} \leq tol_\Theta$ at each node (i, j) of the bearing surface mesh;
- Once the convergence condition is satisfied, the pressure profile can be determined using Equation (9) and the bearing characteristics can be deduced.

The process described above corresponds to the resolution of direct problem whose eccentricity ratio ε is known, for the inverse problem which consist of determining the position (the relative position ε) of the centre journal in the bearing for an imposed applied load \bar{F} .

The procedure consists of:

- Input initial values of: the eccentricity ratio ε_0 ;
- Solve the direct problem for the value ε_0 ;
- The calculated load carrying capacity \bar{W}_C is compared with the applied load \bar{F} ;
- Calculation of a new eccentricity ratio ε by the method of Brent [46];
- The process stopping after the load convergence condition $\frac{|\bar{W}_C - \bar{F}|}{\bar{F}} \leq tol_W$ is satisfied.

We present, the global computational procedure in the following flowchart (Figure 3).

2.4. Static characteristics of hydrodynamic journal bearing

Performance characteristics of the journal bearing for smooth/textured cases are computed using the following relations:

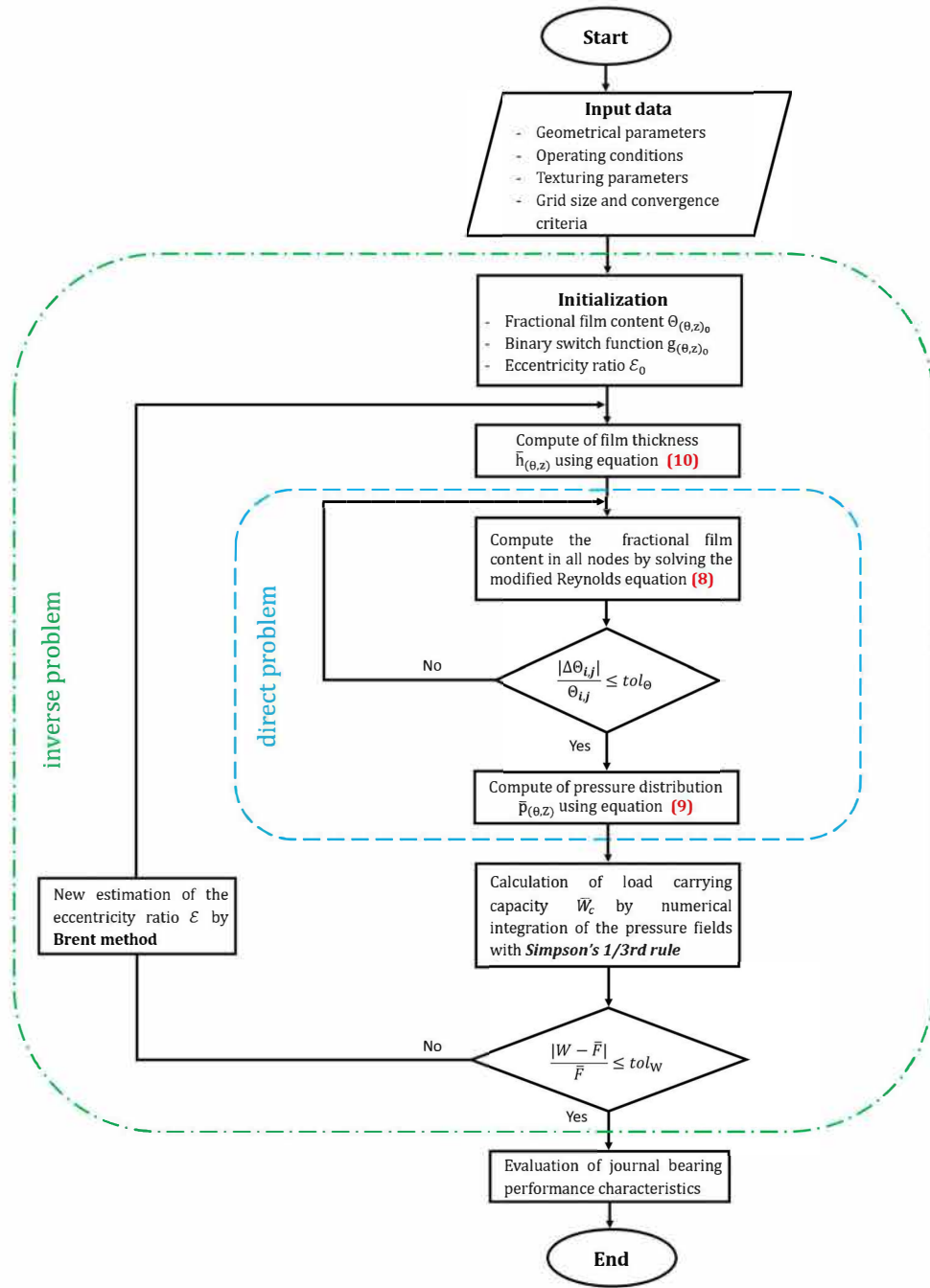


Figure 3. Flowchart for resolution of hydrodynamic problem.

The dimensionless load components in the circumferential and the axial direction are given as:

$$\begin{aligned}\bar{W}_{\theta} &= - \int_0^1 \int_0^{2\pi} \bar{P}_{(\theta,Z)} \cos(\theta) d\theta dZ \\ \bar{W}_Z &= \int_0^1 \int_0^{2\pi} \bar{P}_{(\theta,Z)} \sin(\theta) d\theta dZ\end{aligned}\quad (11)$$

Then the total bearing load capacity and the attitude angle are:

$$\bar{W}_C = \sqrt{\bar{W}_{\theta}^2 + \bar{W}_Z^2} \phi = \arctan\left(\frac{\bar{W}_{\theta}}{\bar{W}_Z}\right) \quad (12)$$

The dimensionless lubricant axial film flow discharging

from the two ends of the bearing, is given by:

$$\bar{Q}_z = \int_0^1 \int_0^{\theta_s} \left(\frac{R}{L}\right)^2 \frac{\partial \bar{P}_{(\theta, end)}}{\partial Z} \bar{h}_{(\theta, end)}^3 \bar{y}(\bar{y} - 1) d\theta d\bar{y} \quad (13)$$

The dimensionless friction torque acting on the journal surface is given by:

$$\begin{aligned}\bar{F}_t &= \int_0^1 \int_0^{\theta_s} \left(\frac{1}{2} \frac{\partial \bar{P}_{(\theta,Z)}}{\partial \theta} \bar{h}_{(\theta,Z)} + \frac{1}{\bar{h}_{(\theta,Z)}} \right) d\theta dZ \\ &+ \int_0^1 \int_{\theta_s}^{2\pi} \frac{\bar{h}_{(\theta,Z)}}{\bar{h}_{(\theta,Z)}^2} d\theta dZ\end{aligned}\quad (14)$$

Where, $\bar{h}_{(\theta,Z)}$ is the equivalent of oil film thickness in cavitation zone.

Table 3. Comparison of performance characteristics of smooth journal bearing.

		Present study	Jang and Khonsari [47]
Eccentricity ratio	ε	0.395	0.392
Maximum pressure	P_{\max} (MPa)	5.799	5.90
Leakage flow-rate	Q (cm ³ /s)	3.153	2.9
Attitude angle	ϕ°	67.618	69.1
Friction coefficient	f	0.0037	0.0039

Consequently, the frictional coefficient is obtained as follows:

$$f\left(\frac{R}{C}\right) = \frac{\bar{F}_t}{\bar{W}_C} \quad (15)$$

All numerical integrations was carried-out by means of Simpson's 1/3rd rule.

3. Numerical results and discussions

3.1. Preliminary validation

Based on the analysis described in the present paper, a Matlab computer program was developed. This section is devoted to the validation of our code. To this end, a comparison analysis is performed between our results and those from researchers works [24,47], for smooth/textured surfaces of the bearings.

Case 1: Smooth surface

Parameters adopted for this comparison are:

- Bearing data: (a) amplitude of external load $F = 20000$ N; (b) journal diameter $D = 40$ mm; (c) bearing length $L = 80$ mm; (d) radial clearance $C = 30$ μ m; (e) Shaft speed $N = 2500$ rpm; (f) lubricant viscosity $= 0.02$ Pa s; (g) bulk modulus $\beta = 5$ GPa.
- Computational method parameters: (a) finite-difference method (FDM) with JFO boundary conditions (b) grid size (91, 41); (c) convergence criteria $tol_\theta = 10^{-6}$, $tol_W = 10^{-4}$.

Table 3 presents the comparison between our predictions and those of the already mentioned paper [47]. It can be noted that the obtained values are very close to the reference ones.

The two dimensional results of film thickness, fractional film content and pressure distributions

obtained by the computational code are plotted in Figure 4 in order to further check its validity. Note that, in fractional film content distribution, the area where $\Theta \geq 1$ represents the full film region, and the area where $\Theta \leq 1$ represents the cavitation region; the variation in fractional film content in full film region is very small due to the large bulk modulus. However, a small variation in fractional film content in the full film region causes large change in the pressure distribution, as a results of the large value of the compressibility. Due to the atmospheric pressure imposed on the axial boundary, the fractional film content at $z=0$ and $z=L$ is assumed to be $\Theta = 1$, while on circumferential boundary, is due to the bearing line groove, situated at $\theta = 0^\circ$ and extending at the ends of the bearing.

Case 2: Textured surface

Parameters adopted for this case are:

- Bearing data: (a) amplitude of external load $F = 12600$ N; (b) journal diameter $D = 63$ mm; (c) bearing length $L = 63$ mm; (d) radial clearance $C = 30$ μ m; (e) angular speed $\omega_1 = 625.4$ rad/s; (f) lubricant viscosity $= 0.0035$ Pa s.
- Computational method parameters: (a) finite difference method (FDM) with Reynolds boundary conditions (b) grid size (391, 142); (c) convergence criteria $tol_p = 10^{-4}$ and $tol_W = 10^{-5}$.
- Bearing texture data: (a) spherical texture shape (b) texture radius $r_x = r_z = 5$ mm; (c) texture depth $r_y = 1$ μ m; (d) distribution along: circumferential $nC_\theta = 1, 2, \dots, 9$ and axial $nC_z = 2$ directions.

The comparison results are plotted in Figure 5. The results of the present comparison are in good agreement with one slight difference which may be due to the computational errors in the simulation, especially the choice made concerning the numerical integration method, where in [24] they used the rectangular integration method and in our model we used a more precise method i.e. Simpson's 1/3rd rule.

In order to further show the effectiveness of our computational code, Figure 6 presents the prediction results for the film thickness and the pressure distribution for smooth/textured cases. The results in

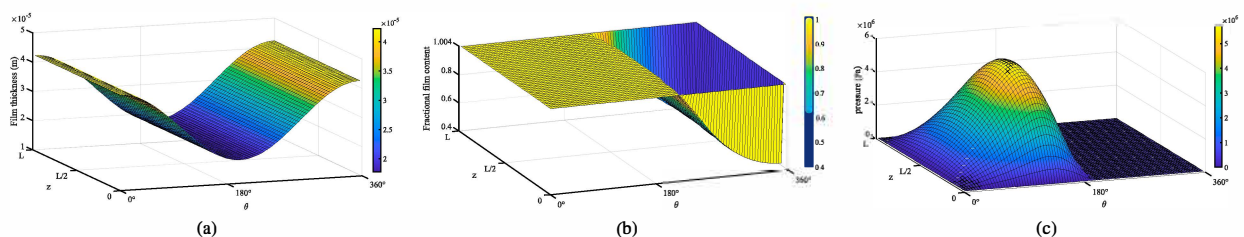


Figure 4. Film thickness evolution, fractional film content and pressure distributions on the contact for the validation case.

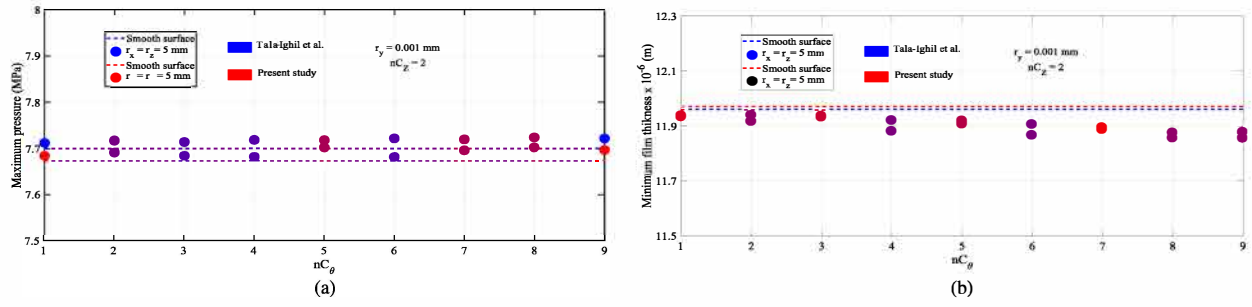


Figure 5. Variation of: (a) maximum pressure; (b) minimum film thickness for smooth and textured surfaces.

Figure 6(b) show very clearly the effect of textures on film thickness evolution and pressure distribution, when compared to smooth case (Figure 6(a)).

3.2. Performance analysis of textured journal bearing

In this section, our objective is to point out the preponderant effect (in terms of tribological properties) between texture contour surface and dimple bottom profile.

Bearing geometrical characteristics, as well as texturing parameters are given in Table 4. Note that, the bearing is with a line groove of negligible thickness, situated at the maximum film thickness and extending at the ends of the bearing.

In the next subsections, the obtained results obtained from the full-textured/smooth bearing cases are compared in terms of: maximum pressure, load carrying capacity, attitude angle, axial film flow, friction coefficient, film rupture angle, film thickness, fractional film content and pressure distributions. Moreover, the choice of the best texture shape depends on the following criteria: the increase in pressure and

load carrying capacity and the decrease in load attitude angle and friction coefficient.

3.2.1. Maximum pressure

The curves of dimensionless maximum pressure \bar{P}_{max} for various eccentricity ratios; are shown in Figure 7 (a,b) (for flat/wedge bottom profile cases). It is found that the rate of increase in \bar{P}_{max} for all considered cases is pronounced at higher values of eccentricity ratio ε . Furthermore, the previous figures also show the comparative graph for smooth/textured surfaces with all studied texture shapes. Maximum pressure values are clearly different from those recorded for the smooth surface. However, it can be seen from Figure 7(a) that the main feature of all texture shapes with flat bottom profiles is to reduce the maximum pressure, which is due to the sudden change in the gap, causes a much large film thickness divergence. In the opposite way, texture shapes with wedge bottom profiles (Figure 7(b)) gradually reduce pressure via their diverging leading wedges. While, the reduction rate of T3 is more severe because it has a longer divergent wedge, which causes the highest film thickness

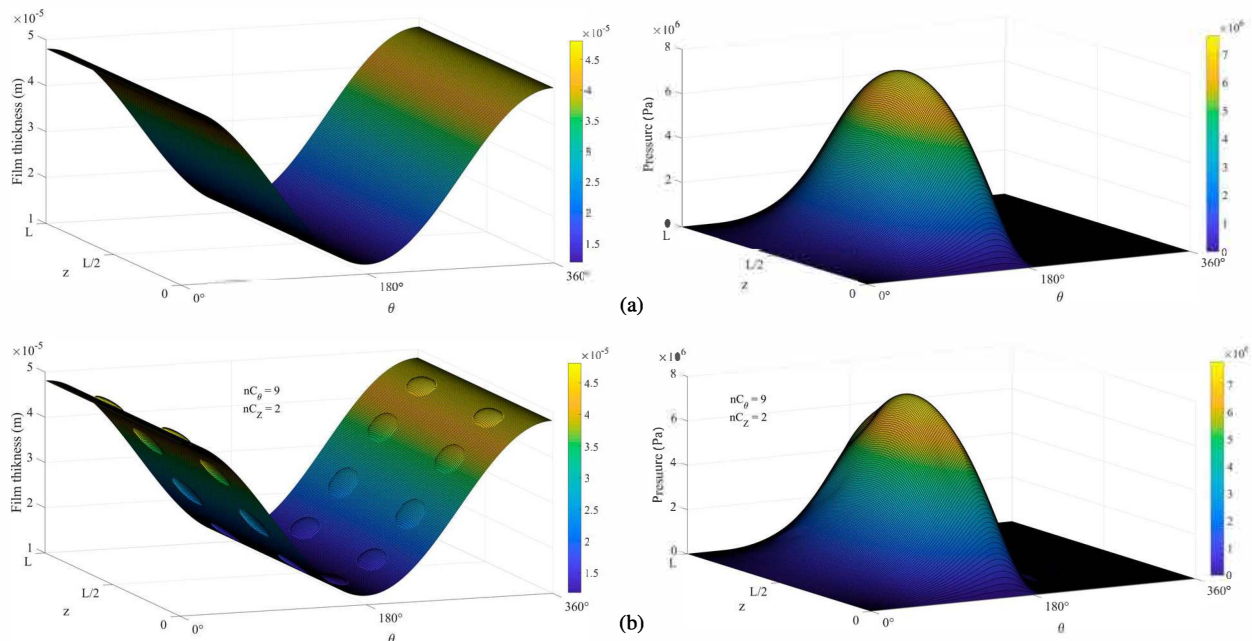


Figure 6. Film thickness evolution and pressure distribution on the contact for smooth/textured journal bearing for the validation case. (a) smooth journal bearing and (b) textured journal bearing.

Table 4. Geometrical and Texturing parameters for the studied journal bearing.

Geometrical parameters			Dimensionless variables	
Shaft diameter	D (mm)	40	L/D	1
Bearing length	L (mm)	40		
Radial clearance	C (μ m)	50		
Eccentricity	e	10–45	e/C	0.2–0.9
Operating conditions				
Journal speed	N (rpm)	3000		
Viscosity	μ (Pa s)	0.05		
Bulk modulus	β (MPa)	100	40	
Texturing parameters				
Texture diameter	r_x (mm)	6	$\bar{r}_x = r_x/R$	0.3
Texture length	r_z (mm)	6	$\bar{r}_z = r_z/L$	0.15
Texture depth	r_y (mm)	15	$\bar{r}_y = r_y/C$	0.3
Texture density	ρ_{tex}		40%	
Texture number along the circumference	nC_θ		14	
Texture number along the length	nC_z		4	
Grid size and convergence criteria				
Nodes per texture along the circumference	nN_{tx}		21	
Nodes per texture along the length	nN_{tz}		19	
Nodes in circumferential direction	nN_θ		441	
Nodes in axial direction	nN_z		121	
Convergence criteria	tol_θ		10^{-8}	

divergence and largest pressure drop. Triangular shape T2 shows a significant increase in the maximum pressure \bar{P}_{max} , this singular behaviour is due to the highest pressure recovery given by the long convergent wedge of this texture shape, which results in shallow pressure drop and highest additional pressure generation in the lubricated area. These results are coherent with the analysis described in [37,38].

3.2.2. Load carrying and attitude angle

Figure 8(a,b) show the variation of dimensionless load carrying capacity \bar{W}_C with eccentricity ratio ϵ ; for smooth and textured profiles. Firstly, the increase in \bar{W}_C has the same behaviour as for the previous dimensionless maximum pressure (Figure 7(a,b)) for smooth and textured cases. Secondly, texturing the whole bearing surface does not enhance the load carrying capacity

except for the T2 texture shape. This enhancement is a consequence of the convergent wedge action provided by T2. This can be explained by the fact that, in full film region, dimple shapes with flat bottoms have a micro-step bearing feature. While, the dimple shapes with micro-wedge has a divergent/convergent wedge (an arc in SP or linear in T1, T2 and T3). Due to these mechanisms, the micro-step bearing causes a much large film thickness divergence, so a significant pressure drop (in full film region) and a smaller pressure recovery will be generated (in rupture film region), which results in a poor load carrying capacity. Note that, the texture contour geometry of the flat bottom profile, in the full film region, has an important effect, as the texture contour geometries increases, the micro-step bearing mechanism effects increases (higher film thickness divergence and larger pressure drop). In one hand, the comparison shown in Figure 8(b), indicates that the same reduction rate in load carrying capacity, compared to the smooth surface, for textured bearing with triangular shape T1 and spherical is observed. This can be justified by the fact that the two shapes are affected by the same mechanism, the micro-wedge action, with a slight difference in geometrical bottom profile (an arc in SP and a broken line in T1). In the other hand, the two extreme trends corresponding to the load carrying capacities of T2 and T3 texture shapes are also due to the micro-wedge action mechanism, which is positive (convergent) in the first case (T2) and negative (divergent) in the second case (T3), these results are consistent with those described in [34,35]. Here, an emphasis is placed on the rotation direction, which present a key parameter in the wedge profile orientation (convergent or divergent).

Figure 9(a,b) present the variation of the load attitude angle ϕ against the eccentricity ratio ϵ for smooth/textured surface bearings. It can be discerned from the figures, that for any texture shapes, the values of load attitude angle are obviously different from those of smooth surfaces. For all studied cases, ϕ decreases with the increase in ϵ , this decrease is more considerable at higher values of eccentricity ratio to support the large bearing load. However, for all considered texture shapes with flat bottom profiles (Figure 9(a)),

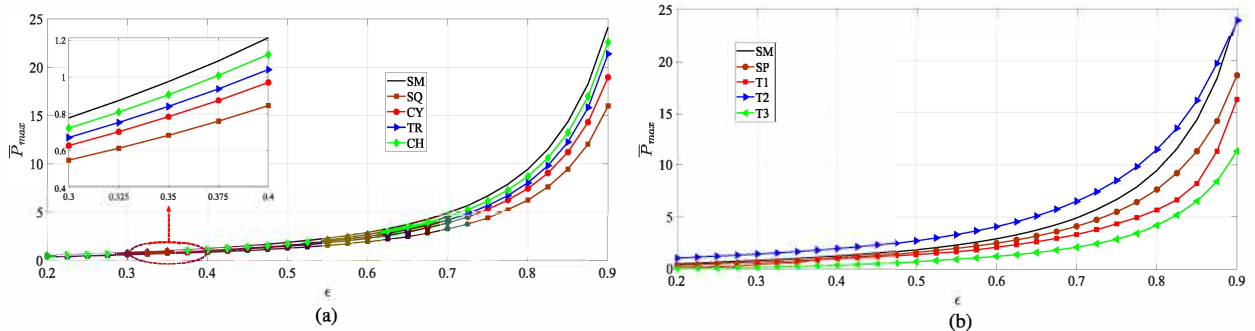


Figure 7. Dimensionless maximum pressure versus eccentricity ratio for smooth/textured surface bearings. (a) flat bottom cases and (b) wedge bottom cases.

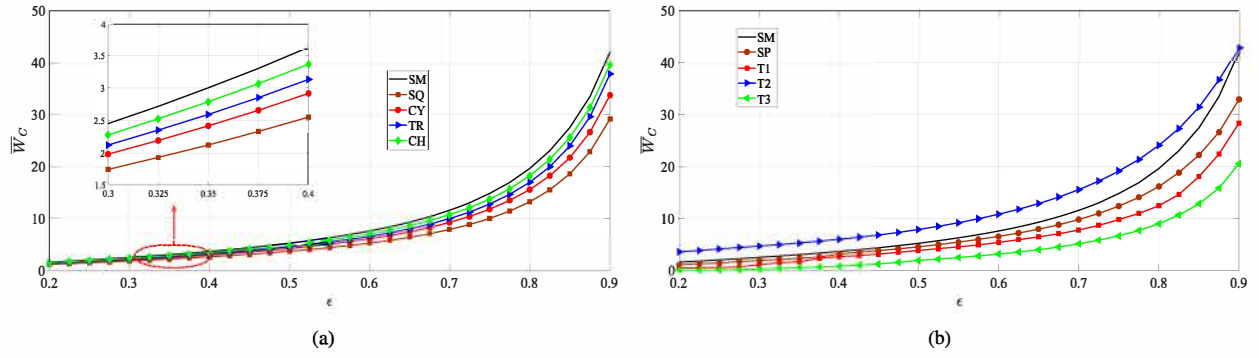


Figure 8. Dimensionless load carrying capacity versus eccentricity ratio for different texture profiles. (a) flat bottom cases and (b) wedge bottom cases.

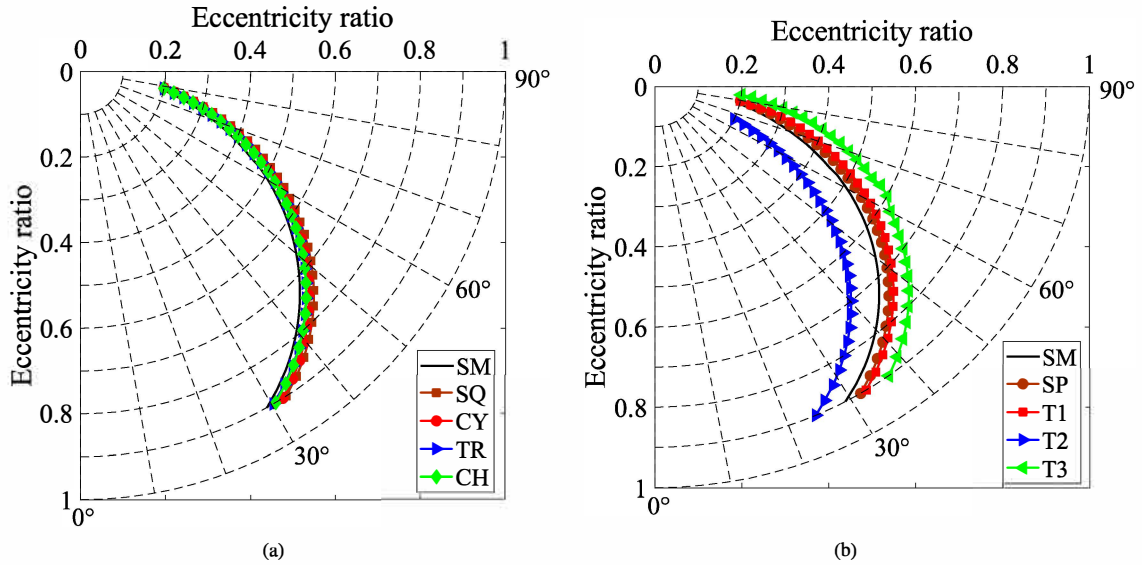


Figure 9. Load attitude angle versus eccentricity ratio for considered texture profiles. (a) Textures with a constant/flat dimple depths and (b) Textures with a variable/wedge dimple depths.

the load attitude angle slightly increases compared to the smooth surface bearing case. These results can be explained by the presence of micro-step bearing mechanism, which causes a pressure drop and makes its distribution more asymmetric on the circumferential direction. In Figure 9(b), the effect of texture bottom profiles on load attitude angle is more noticeable, where, it adopts two different behaviours: increases for spherical and T1 and even more for T3 profiles and decreases for T2, when compared to smooth surface. This is due to the micro-wedge bearing effect, which causes a large pressure drop in the case of divergent bottom profile: spherical, T1 and T3, and a high pressure recovery in the case of convergent bottom: T2, giving more symmetric pressure distribution on the circumferential direction, and leading towards nil load attitude angle.

3.2.3. Axial film flow

The evolution of the dimensionless axial film flow \bar{Q}_z for different values of eccentricity ratio ϵ in the cases of smooth and textured surface bearing are shown in Figure 10(a,b). In Figure 10(a), it is noticed that for

all considered configurations (smooth and textured surface bearing with constant/flat dimple depths), the axial film flow increases with the increase of ϵ , which can be justified by the large pressure gradient on the both ends, and it is also visible that textures with flat bottom profiles reduce the axial film flow, as a result of micro-step bearing mechanism effects. In Figure 10(b), the same evolution is observed for all texture shapes with wedge bottom profiles except for T2 texture, which has an important axial flow when the eccentricity ratio is less than 0.75, and decreases for $\epsilon > 0.75$, compared to smooth bearing case.

This can be explained by the fact that, at low eccentricity ratios, the additional hydrodynamic pressure generated by the long convergent wedges of the triangular T2 textures in the lubricated area is more important, which increases the bearing pressure gradient and so increases the axial film flow. At high eccentricity ratios ($\epsilon > 0.75$) the effect of T2 texture shape is negligible when compared with the effect of bearing convergent zone, in this case, the T2 texture shape adopt the same behaviour as the other textures.

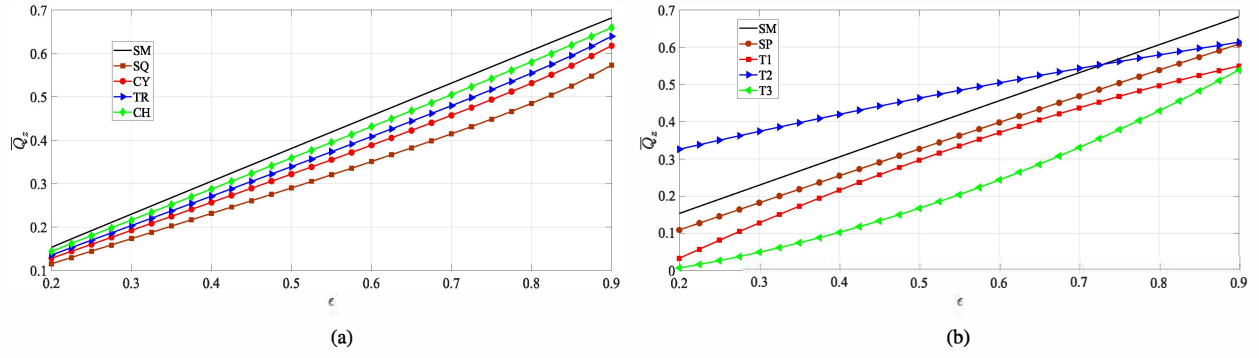


Figure 10. Dimensionless axial flow versus eccentricity ratio for different texture profiles. (a) Textures with a constant/flat dimple depths and (b) Textures with a variable/wedge dimple depths.

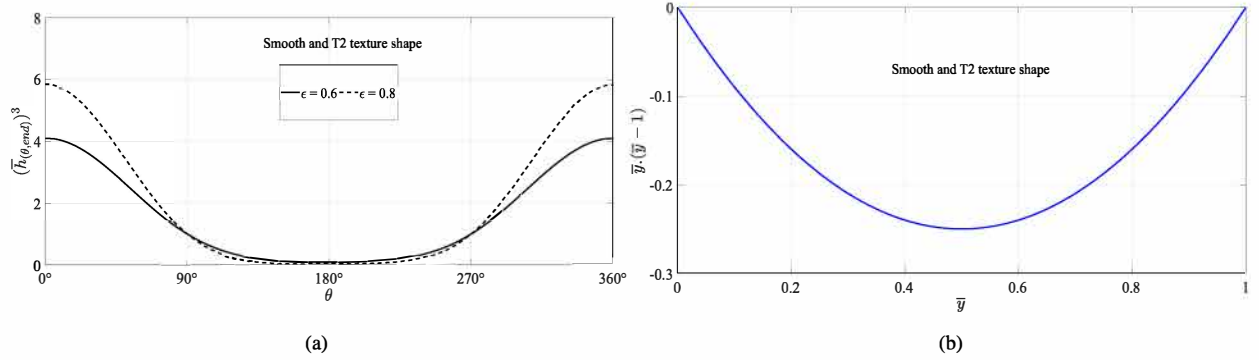


Figure 11. Variation curves of the dimensionless oil film thickness and radial direction components at the bearing end for various eccentricity ratios. (a) dimensionless oil film thickness and (b) dimensionless radial direction.

In order to clarify the previous behaviour of T2 texture, a variation analysis of the main components of axial film flow Equation (13) (pressure gradient $\frac{\partial \bar{P}_{(\theta, end)}}{\partial Z}$, film thickness $\bar{h}_{(\theta, end)}^3$, radial direction $\bar{y}(\bar{y} - 1)$) will be presented in Figures 11 and 12.

Figure 11(a,b) show the variation curves of the dimensionless oil film thickness and radial direction components, respectively, for smooth and T2 texture shape at various eccentricity ratios ($\epsilon = 0.6$ and $\epsilon = 0.8$). It should be emphasized that, results in Figure 11(a) is concern the bearing end at $z = L$, which is the same in both cases (smooth and T2 texture shape), while in Figure 11(b), results are about the variable \bar{y} (dimensionless distance between the shaft and the bearing ranging on $[0, 1]$) which

makes it independent to the surface's nature and the eccentricity ratios.

The curves of dimensionless pressure gradient at bearing end is presented in Figure 12(a) for smooth and T2 texture shape, at $\epsilon = 0.6$ and $\epsilon = 0.8$, it is well observed that the areas under the curves of T2 are important compared to smooth case, which in the fact, confirms the previous finding of dimensionless maximum pressure (Figure 7(b)) and load capacity (Figure 8(b)).

The variation of the dimensionless axial film flow gradient, which is in fact resulting from the multiplication of the previous components entities, is shown in Figure 12(b). It is noticed that, at $\epsilon = 0.6$; the area in the case of smooth surface is under

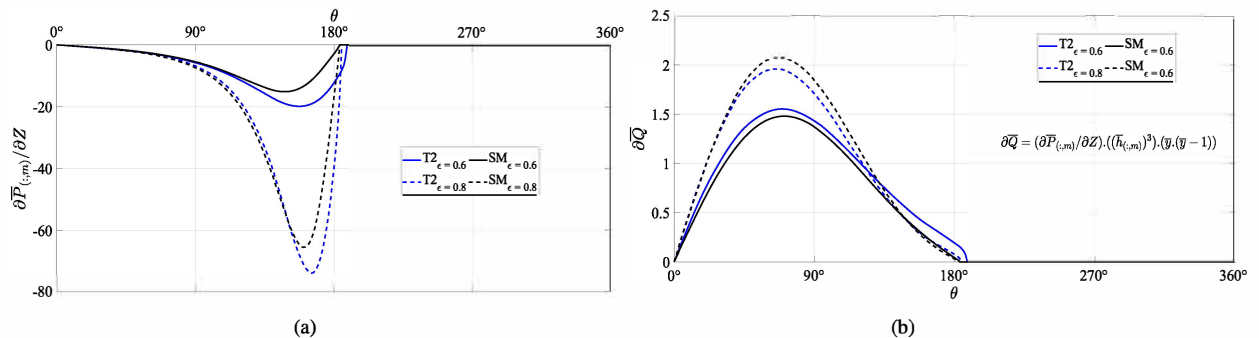


Figure 12. Variation of the dimensionless pressure gradient and axial film flow gradient component at the bearing end for smooth surface and T2 texture shape. (a) dimensionless pressure gradient and (b) dimensionless axial film flow gradient.

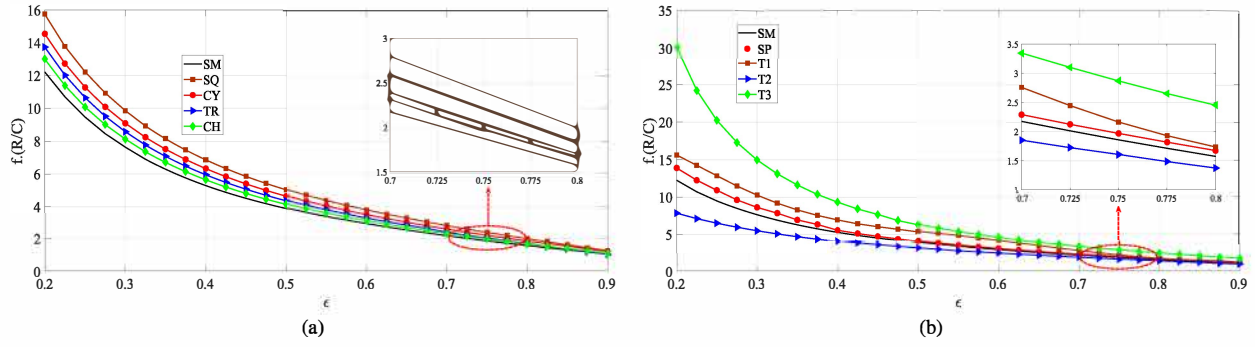


Figure 13. Friction coefficient versus eccentricity ratio for studied texture profiles. (a) flat bottom cases and (b) wedge bottom cases.

the curve of T2 texture shape, but at $\varepsilon = 0.6$ a reverse behaviour is noted; which explain and correspond well to the results already expressed in Figure 10(b).

3.2.4. Friction coefficient

The dimensionless friction coefficients $f. (R/C)$ for smooth/textured surface bearings are plotted in Figure 13(a) (for flat/wedge bottom profile cases, respectively). It can be noticed that, compared to the maximum pressure (Figure 7(a,b)) and load carrying capacity (Figure 8(a,b)), the resulting friction coefficients values have an opposite trend. Moreover, it can be also observed that, the friction coefficient $f. (R/C)$ decreases with the increases of eccentricity ratio ε , for all studied cases. However, in the case of textured bearings with flat bottom profiles, the friction coefficients shallowly increases compared to the smooth surface case, presenting a bad performance. This is due to the fact that the flat bottom profiles causes a pressure drop, which decreases the load carrying capacity, and so increases the friction values. In the other case of textured bearings with wedge bottom profiles, the triangular shape T2 with convergent (positive) wedge action shows the greatest friction reduction. This is due to the increase in load carrying capacity, caused by the highest pressure recovery. The triangular shape T3 with divergent (negative) wedge action performs the worst friction value.

In the following sections, the eccentricity ratio will be fixed at $\varepsilon = 0.6$, in order to present properly the results of film thickness evolution, fractional film content distribution and pressure distributions.

3.2.5. Film thickness, fractional film content and pressure distributions

For the sake of clear representation, Figure 14 shows the three-dimensional distribution of lubricant film thickness computed at the contact interface for all studied cases. This figure shows that the film thickness evolution for smooth (Figure 14(a)) and textured (with flat, Figure 14(b), and wedge, Figure 14(c), bottom profiles) surface bearings remain constant in the

axial direction, and, its minimum value occurs near $\theta = 181^\circ$.

Figure 15 shows the variation of fractional film content in circumferential (at the mid-plane) direction, for smooth and textured surface bearing, with constant (flat bottom) and variable (wedge bottom) dimple depths. In the case of texture shapes with flat bottom profiles (Figure 15(a)), it can be seen that all curves of texture fractional film content are less than the smooth surface, as a results of micro-pressure drop effect of these textures, it is also very clear that as the texture contour geometry increases, the micro-pressure drop effect increases. Unlike the previous case, a considerable effect of texture shapes with wedge bottom profiles (Figure 15 (b)) on fractional film content is clearly noticed, especially in the case of triangular shape T2, which presents a significant improvement in the film fluid area (increasing the value of rupture angle).

The effect of texture shapes with flat/wedge bottom profiles on the dimensionless pressure profile is visualized in Figure 16(a,b), respectively. Each figure is plotted in circumferential (at the mid-plane, case (c)) and axial (at the maximum pressure plane θ_p° , case (d)) directions. The dimensionless film pressure for all texture shapes with flat bottom profiles (Figure 16(a)) are less than the smooth surface film pressure, which confirm the influence of micro-step bearing mechanism. Moreover, it can be noticed that the maximum pressure plane for all textures profiles is constant at $\theta_p^\circ = 146.45^\circ$.

The results shown in Figures 16(b) for all texture shapes with wedge bottom profiles are the same as in the previous figure, except for some minor differences:

- The dimensionless pressure profile and the rupture angle of T2 texture shape are sharply higher than other cases,
- Some fluctuations appeared on the T1 and T2 pressure profiles,
- The maximum pressure planes θ_p° increase in the case of triangular texture shape with convergent

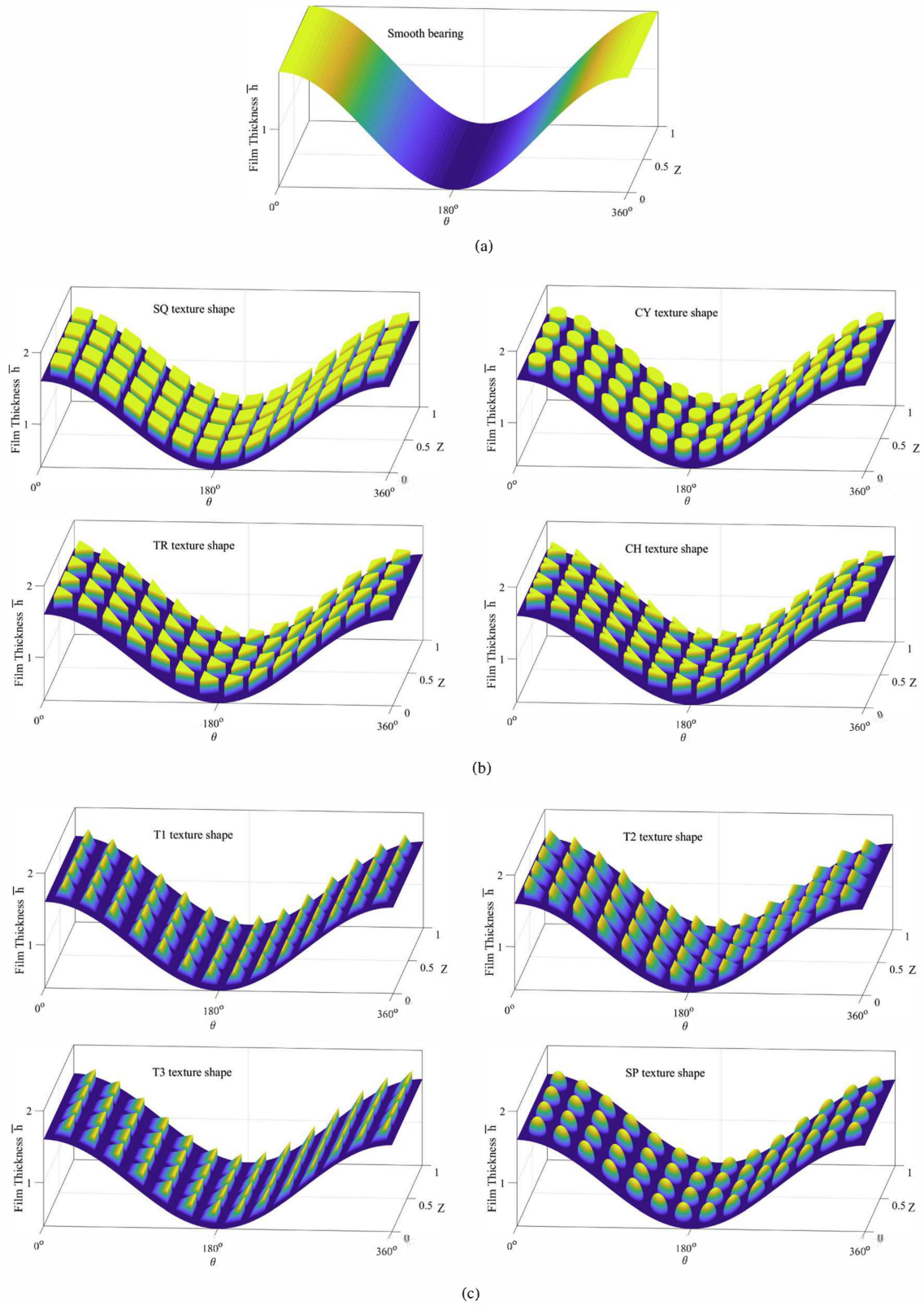


Figure 14. Evolution of dimensionless film thickness versus axial and circumferential coordinates for smooth and different texture profiles. (a) smooth surface bearing, (b) flat bottom profile cases and (c) wedge bottom profile cases.

wedge T2 and decrease in T3 triangular texture shape with divergent wedge.

These differences are due to the convergent and/or divergent wedge bottom profiles micro-wedge bearing mechanism, that directly affect the pressure distribution.

3.3. Effect of texture density and location

In the previous sections, the whole bearing surface was textured (from 0° to 360°) and the texture density ρ_{tex} , which is the surface occupied by dimples units per the total bearing surface, was set to 40%. Here, two texture configurations (Figure 2) and four texture densities are

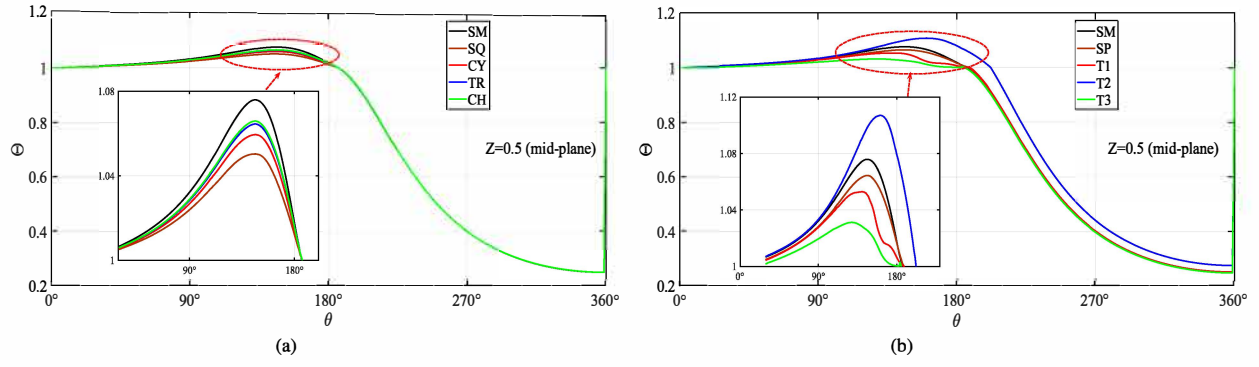


Figure 15. Effect of various texture shapes with a flat bottom profile on fractional film content distribution along the circumferential direction at bearing mid-plane. (a) flat bottom cases and (b) wedge bottom cases.

considered, including the previous one of 40% and 20%, 60% and 80%. Computed characteristics corresponding to each texture density are summarized in Table 5. In full textured cases, the result observed is that: except T2 texture shape, all textures have a detrimental effect (reducing the load carrying capacity and increasing the friction coefficient). Where, for flat bottom profiles, the square texture performs the worst effect, due to the larger contour geometry followed by the circle, triangle and chevron. While, in wedge bottom profiles, T2 performs the best and T3 the worst, as a results of convergent/divergent wedge profiles, which can positively or negatively affects the tribological characteristics of the journal bearing. This was confirmed by simulation results shown in Figures 7–16, where T2 and T3 have the highest and lowest effects, respectively. Moreover, as the texture density increases, the micro-step and micro-wedge bearing

mechanism effects increases. In partial-texturing cases, (from 180° to 360°), all texture shapes with constant dimple depths perform better by increasing the load lifting capacity and lowering the friction coefficient, and is more pronounced at higher texture densities. Due to, no pressure drop (in full film region) and a smaller pressure recovery generated (in rupture film region) by micro-step mechanism. Square texture shape performed the best hydrodynamic enhancement, followed by the triangle and circle, which confirms the results obtained by Zhang et al. [42]. For textures with variable dimple depths, the micro-wedge mechanism of convergent profile causes a large micro-pressure recovery and so enhance the bearing performances.

It was found, from this numerical study, that the wedge effect and the micro-step bearing of full/partial texturing feature are a key parameters in the journal

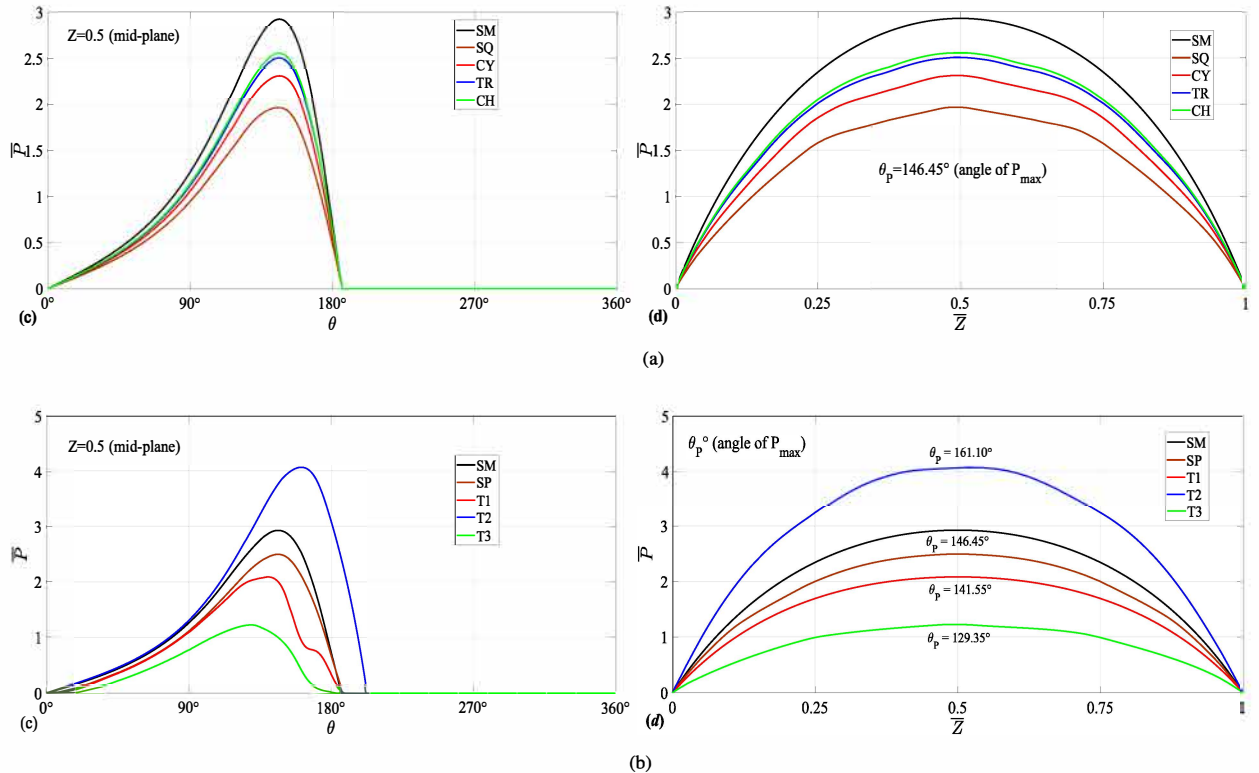


Figure 16. Effect of various texture shapes with a flat/wedge bottom profiles on dimensionless pressure profile. (a) flat bottom profile and (b) wedge bottom bottom profile.

Table 5. Variation of tribological characteristics for full/partial textured bearings with different texture densities.

$L/D = 1$			$\varepsilon = 0.6$								
			20	40	60	80					
$P_{\text{texture}}\%$			10	14	17	18	5	7	8	9	
nC_{θ}			3	4	5	6	3	4	5	6	
SM	Load carrying capacity	Full textured	7,560				Partial textured (from 180° to 360°)	7,560			
SQ			6,153	5.223	4.073	3.228		7,578	7.6117	7.918	7.951
CY			6.630	6.047	5.296	4.783		7.565	7.581	7.667	7.792
TR			6.889	6.515	5.878	5.616		7.574	7.6103	7.779	7.799
CH			6.977	6.638	6.144	5.883		7.570	7.591	7.691	7.797
T1			6.994	6.467	5.864	5.659		7.543	7.530	7.491	7.3025
T2			8.386	10.793	11.265	11.546		7.585	8.866	9.440	11.075
T3			5.283	3.134	2.338	1.730		7.534	7.526	7.488	7.300
SP			7.191	6.614	6.274	5.715		7.557	7.541	7.539	7.449
SM	Friction coefficient	Full textured	3.403				Partial textured (from 180° to 360°)	3,403			
SQ			3.736	3.907	4.913	5.730		3.265	2.878	2.702	2.577
CY			3.671	3.835	4.131	4.369		3.332	3.059	2.831	2.797
TR			3.586	3.668	3.908	3.859		3.314	2.791	2.762	2.755
CH			3.561	3.636	3.798	3.859		3.343	2.998	2.824	2.787
T1			3.633	4.629	5.112	5.664		3.799	3.834	3.859	3.861
T2			2.639	2.519	2.149	2.109		2.881	2.501	2.377	2.052
T3			3.895	4.975	6.574	9.133		3.813	3.818	3.837	3.861
SP			3.511	3.913	4.579	5.116		3.818	3.833	3.865	3.889

bearing performances. The same observation has been made for other types of seals in several works [34–38,48]. Wedge effect mechanism (micro-wedge action) has produced tangible results in the particular case of textures with variable dimple depths or wedge bottom profiles (SP, T1, T2 and T3 shapes). A pressure reduction has been noticed for textures with divergent wedge profiles (SP, T1 and T3), while the opposite trend is observed for texture with convergent wedge shape (T2). The produced pressure in T2 texture shape enhances the load lifting capacity, while the divergent film in other textures causes a net load loss. Micro-step bearing mechanism, with the right arrangement of textures on the contact surface, can significantly enhance the bearing performances, by the effect of texture micro-pressure recovery mechanism.

4. Conclusion

In this paper, a numerical study was conducted to highlight the potential of surface texturing on journal bearing performances. Texture shapes with (1) flat bottoms: square, cylinder, triangle (TR) and chevron; and (2) wedge bottoms: triangular (T1, T2, T3) and sphere were considered. The computational model employed herein was solved by means of finite difference technique with taking into account the lubrication film rupture and reformation by adopting the mass-conserving cavitation algorithm ('JFO' boundary conditions). The simulations made with our numerical model were compared to the existing theoretical data, available in the literature.

The findings from the present numerical investigation can be summarized in the following points:

- (1) The geometric shape of the texture has proved to be a key parameter in journal bearing performances.

- (2) Fully textured bearing with flat/constant bottom dimples slightly affect the main performances as compared to the smooth bearing case, which can be explained by the effect of micro-step mechanism (micro-pressure drop effect). Moreover, as the texture contour geometry increases, this mechanism effect increases. While, textures with wedge/variable bottom profiles significantly influence all bearing characteristics, which is directed by the micro-wedge mechanism effect.
- (3) Partial textured cavitation bearing area with constant dimple depths enhance the load lifting capacity and lower the friction coefficient, due to the effect of micro-pressure recovery mechanism. These facts were more noticeable at high texture densities. While, textures with divergent bottom profiles causes a net load loss.
- (4) Among all considered cases of texture shape, T2 appears to be the most favourable to improve the bearing performances; e.g. for a texture density of 40%, it increases the pressure field by a factor of 5 to 6 over the value of the smooth one which in turn increases by 43% the load carrying capacity and decreases the friction coefficient by 26%. While T3 texture shape, presents the worst performances.
- (5) The previous observations concerning T2 texture shape are due to the convergent wedge effect, while, texturing the second angular part of the bearing (beyond 180°) by textures with flat bottom profiles, are due to the micro-pressure recovery effect, which generates additional hydrodynamic pressure and serve as fluid reservoirs that provides lubricant to the contact in starvation cases, and so, enhance the main bearing performances.
- (6) The square 'SQ' texture shape appears to be the most favourable to improve the bearing performances, followed by the triangular 'TR' then chevron 'CH' and cylindrical 'CY'.

This study is restricted to the selected texturing parameters; fixed density, number, disposition, orientation and dimension; and the chosen problem assumptions; by applying Newtonian rheology and mass-conserving cavitation and neglecting changes in viscosity, density and temperature, etc. On one hand, breaking these constraints will open to us new possibilities of finding the optimum texture shapes, on the other hand, difficulties on the computational aspect will be faced (CPU-time and cost). In this context, the application of model order reduction (MOR) [49] for the simulation of textured journal bearing is planned as the next step of this research.

Disclosure statement

No potential conflict of interest was reported by the authors.

ORCID

B. Manser  <http://orcid.org/0000-0001-5901-0527>

I. Belaidi  <http://orcid.org/0000-0003-3463-0580>

A. Hamrani  <http://orcid.org/0000-0002-0295-855X>

S. Khelladi  <http://orcid.org/0000-0002-2095-1087>

F. Bakir  <http://orcid.org/0000-0003-0837-0260>

References

- [1] Frene J, Nicolas D, Degueurce B. Hydrodynamic lubrication: bearings and thrust bearings. Amsterdam: Elsevier; 1997.
- [2] Qiu M, Minson BR, Raeymaekers B. The effect of texture shape on the friction coefficient and stiffness of gas-lubricated parallel slider bearings. *Tribol Int.* 2013;67:278–288.
- [3] Khatri CB, Sharma SC. Influence of textured surface on the performance of non-recessed hybrid journal bearing operating with non-newtonian lubricant. *Tribol Int.* 2016;95:221–235.
- [4] Etsion I. State of the art in laser surface texturing. *Trans ASME-F-J Tribol.* 2005;127(1):248.
- [5] Wang X, Kato K. Improving the anti-seizure ability of sic seal in water with rie texturing. *Tribol Lett.* 2003;14(4):275–280.
- [6] Stephens LS, Siripuram R, Hayden M, et al. Deterministic micro asperities on bearings and seals using a modified liga process. In: ASME turbo expo 2002: power for land, sea, and air. American Society of Mechanical Engineers; 2002. p. 573–580.
- [7] Schneider YG. Formation of surfaces with uniform micropatterns on precision machine and instruments parts. *Precis Eng.* 1984;6(4):219–225.
- [8] Greco A, Raphaelson S, Ehmann K, et al. Surface texturing of tribological interfaces using the vibromechanical texturing method. *J Manuf Sci Eng.* 2009;131(6):061005.
- [9] Wakuda M, Yamauchi Y, Kanzaki S, et al. Effect of surface texturing on friction reduction between ceramic and steel materials under lubricated sliding contact. *Wear.* 2003;254(3):356–363.
- [10] Etsion I. Improving tribological performance of mechanical components by laser surface texturing. *Tribol Lett.* 2004;17(4):733–737.
- [11] Feldman Y, Kligerman Y, Etsion I. A hydrostatic laser surface textured gas seal. *Letters Tribol Lett.* 2006;22(1):21–28.
- [12] Kligerman Y, Etsion I. Analysis of the hydrodynamic effects in a surface textured circumferential gas seal. *Tribol Trans.* 2001;44(3):472–478.
- [13] Ronen A, Etsion I, Kligerman Y. Friction-reducing surface-texturing in reciprocating automotive components. *Tribol Trans.* 2001;44(3):359–366.
- [14] Hamilton DB, Walowit JA, Allen CM. A theory of lubrication by micro-irregularities. *J Basic Eng.* 1966;88(1):177–185.
- [15] Wakuda M, Yamauchi Y, Kanzaki S, et al. Effect of surface texturing on friction reduction between ceramic and steel materials under lubricated sliding contact. *Wear.* 2003;254(3):356–363.
- [16] Pettersson U, Jacobson S. Influence of surface texture on boundary lubricated sliding contacts. *Tribol Int.* 2003;36(11):857–864.
- [17] Varenberg M, Halperin G, Etsion I. Different aspects of the role of wear debris in fretting wear. *Wear.* 2002;252(11):902–910.
- [18] Yamakiri H, Sasaki S, Kurita T, et al. Effects of laser surface texturing on friction behavior of silicon nitride under lubrication with water. *Tribol Int.* 2011;44(5):579–584.
- [19] Etsion I, Kligerman Y, Halperin G. Analytical and experimental investigation of laser-textured mechanical seal faces. *Tribol Trans.* 1999;42(3):511–516.
- [20] Etsion I, Halperin G, Brizmer V, et al. Experimental investigation of laser surface textured parallel thrust bearings. *Tribol Lett.* 2004;17(2):295–300.
- [21] Kovalchenko A, Ajayi O, Erdemir A, et al. The effect of laser surface texturing on transitions in lubrication regimes during unidirectional sliding contact. *Tribol Int.* 2005;38(3):219–225.
- [22] Lu X, Khonsari MM. An experimental investigation of dimple effect on the stribek curve of journal bearings. *Tribol Lett.* 2007;27(2):169–0.
- [23] Tala-Ighil N, Fillon M. A numerical investigation of both thermal and texturing surface effects on the journal bearings static characteristics. *Tribol Int.* 2015;90:228–239.
- [24] Tala-Ighil N, Maspeyrot P, Fillon M, et al. Effects of surface texture on journal-bearing characteristics under steady-state operating conditions. *Proc Inst Mech Eng, J: J Eng Tribol.* 2007;221(6):623–633.
- [25] Ausas R, Ragot P, Leiva J, et al. The impact of the cavitation model in the analysis of microtextured lubricated journal bearings. *J Tribol.* 2007;129(4):868–875.
- [26] Elrod HG, Adams MLT. A computer program for cavitation and starvation problems. *Cavitation and Related Phenomena in Lubrication.* 1974;103:37–41.
- [27] Kango S, Sharma RK, Pandey RK. Thermal analysis of microtextured journal bearing using non-newtonian rheology of lubricant and jfo boundary conditions. *Tribol Int.* 2014;69:19–29.
- [28] Kango S, Sharma RK, Pandey RK. Comparative analysis of textured and grooved hydrodynamic journal bearing. *Proc Inst Mech Eng, Part J: J Eng Tribol.* 2014;228(1):82–95.
- [29] Zhang H, Dong G, Hua M, et al. Parametric design of surface textures on journal bearing. *Ind Lubr Tribol.* 2015;67(4):359–369.
- [30] Anno JN, Walowit JA, Allen CM. Microasperity lubrication. *J Lubr Technol.* 1968;90(2):351–355.

- [31] Etsion I, Burstein L. A model for mechanical seals with regular microsurface structure. *Tribol Trans.* **1996**;39(3):677–683.
- [32] Tønder K. Inlet roughness tribodevices: dynamic coefficients and leakage. *Tribol Int.* **2001**;34(12):847–852.
- [33] Tønder K. Hydrodynamic effects of tailored inlet roughnesses: extended theory. *Tribol Int.* **2004**;37(2):137–142.
- [34] Olver AV, Fowell MT, Spikes HA, et al. Inlet suction, a load support mechanism in non-convergent, pocketed, hydrodynamic bearings. *Proc Inst Mech Eng, Part J: J Eng Tribol.* **2006**;220(2):105–108.
- [35] Fowell M, Olver AV, Gosman AD, et al. Entrainment and inlet suction: two mechanisms of hydrodynamic lubrication in textured bearings. *J Tribol.* **2007**;129(2):336–347.
- [36] Yagi K, Sugimura J. Balancing wedge action: a contribution of textured surface to hydrodynamic pressure generation. *Tribol Lett.* **2013**;50(3):349–364.
- [37] Nanbu T, Ren N, Yasuda Y, et al. Micro-textures in concentrated conformal-contact lubrication: effects of texture bottom shape and surface relative motion. *Tribol Lett.* **2008**;29(3):241–252.
- [38] Uddin MS, Ibatan T, Shankar S. Influence of surface texture shape, geometry and orientation on hydrodynamic lubrication performance of plane-to-plane slider surfaces. *Lubr Sci.* **2017**;29(3):153–181.
- [39] Jakobsson B. The finite journal bearing considering vaporization. *Trans. Chalmers Univ. of Tech, Sweden*; 1965. p. 190.
- [40] Olsson K-O. Cavitation in dynamically loaded bearing. *Trans. Chalmers Univ. of Tech, Sweden*; 1957. p. 308.
- [41] Vijayaraghavan D, Keith TG. An efficient, robust, and time accurate numerical scheme applied to a cavitation algorithm. *J Tribol.* **1990**;112(1):44–51.
- [42] Zhang YL, Zhang XG, Matsoukas G. Numerical study of surface texturing for improving tribological properties of ultra-high molecular weight polyethylene. *Biosurf Biotribol.* **2015**;1(4):270–277.
- [43] Tala-Ighil N, Fillon M, Maspeyrot P. Effect of textured area on the performances of a hydrodynamic journal bearing. *Tribol Int.* **2011**;44(3):211–219.
- [44] Dobrica MB, Fillon M, Pascovici MD, et al. Optimizing surface texture for hydrodynamic lubricated contacts using a mass-conserving numerical approach. *Proc Inst Mech Eng, Part J: J Eng Tribol.* **2010**;224(8):737–750.
- [45] Fesanghary M, Khonsari MM. A modification of the switch function in the elrod cavitation algorithm. *J Tribol.* **2011**;133(2):024501.
- [46] Press WH. *The art of scientific computing*. New York: Cambridge University Press; **1992**.
- [47] Jang JY, Khonsari MM. On the behavior of misaligned journal bearings based on mass-conservative thermohydrodynamic analysis. *J Tribol.* **2010**;132(1):011702.
- [48] Yu H, Wang X, Zhou F. Geometric shape effects of surface texture on the generation of hydrodynamic pressure between conformal contacting surfaces. *Tribol Lett.* **2010**;37(2):123–130.
- [49] Cherabi B, Hamrani A, Belaidi I, et al. An efficient reduced-order method with pgd for solving journal bearing hydrodynamic lubrication problems. *Comptes Rendus Mécanique.* **2016**;344(10):689–714.

Appendix

e	Eccentricity (m)
C	Radial clearance (m)
D	Bearing diameter (m)
L	Bearing length (m)
R	Bearing radius (m)
F	External applied force (N)
u, w	Velocity components in directions θ and Z .
x, y, z	Global coordinate system (m)
r_x, r_z, r_y	Texture dimensions (m)
h	Film thickness (m)
Δh	Variation of film thickness due to the presence of the texture (m)
p	Lubricant pressure (Pa)
p_c	Cavitation pressure (Pa)
p_{max}	Maximum pressure (Pa)
W_c	Load carrying capacity
S	Sommerfeld number
Q_z	Axial film flow (m ³ /s)
F_t	Friction force (N.m)
f (R/C)	Friction coefficient
g	Cavitation switching function
nC_θ, nC_z	Number of textures along circumferential θ and axial Z directions
tol_θ	Relative convergence criterion on pressure
tol_w	Relative convergence criterion on load
\bar{p}_{max}	Dimensionless maximum pressure
\bar{p}_c	Dimensionless cavitation pressure
\bar{W}_c	Dimensionless load carrying capacity
\bar{u}, \bar{w}	Dimensionless velocity components in directions θ and Z .
\bar{Q}_z	Dimensionless axial film flow
\bar{F}_t	Dimensionless friction force
\bar{h}	Dimensionless film thickness [h/C]
\bar{h}_s	Dimensionless equivalent of oil film thickness in cavitation zone
$\Delta \bar{h}$	Dimensionless variation of film thickness due to the presence of the texture
\bar{p}	Dimensionless lubricant pressure
θ, \bar{y}, Z	Dimensionless global coordinate system
$\bar{r}_x, \bar{r}_z, \bar{r}_y$	Dimensionless texture dimensions
ρ_{tew}	Texture density
ρ	Fluid density of the oil (kg/m ³)
ρ_c	Fluid density at the cavitation pressure (kg/m ³)
β	Bulk modulus (Pa)
$\bar{\beta}$	Dimensionless bulk modulus
Θ	Fractional film content $\Theta = \rho/\rho_c$
τ_{xy}	Shearing stresses (Pa)
ϕ	Attitude angle (deg)
ω	Angular velocity (rad/s)
μ	Dynamic viscosity (Pa s)
ε	Relative eccentricity
θ_s	Angular position of the rupture zone (deg)
θ_p	Angular position of maximum pressure (deg)